

Shear localization and damage in metallic glasses at high homologous temperatures

R. Ekambaram^a, P. Thamburaja^{a,*}, Nikabdullah^b

^aDepartment of Mechanical Engineering, National University of Singapore, Singapore 117576

^bDepartment of Mechanical Engineering, Universiti Kebangsaan Malaysia, Bangi, Malaysia 43600

Abstract

Studies of shear localization and fracture behavior in bulk-metallic glasses (BMGs) have been primarily limited to temperature regimes well-below the glass transition temperature. In this work, we investigate the shear localization and damage behavior of BMGs at temperatures within the supercooled liquid region where manufacturing processes of components made out of BMGs typically take place.

To model the deformation behavior of BMGs, we use the constitutive model developed by Thamburaja and Ekambaram (2007) and augment it to include a damage/fracture criterion. The modified constitutive model is then implemented in the ABAQUS (2008) finite-element program by writing a user-material subroutine. The material parameters in the constitutive model is then fitted to stress-strain curves obtained from a set of simple compression experiments conducted by Lu *et al.* (2003) under various strain-rates at an ambient test temperature within the supercooled liquid region. With the model calibrated, we study the shear localization and damage behavior of the aforementioned Zr-based BMG by performing FEM simulations at various temperatures within the supercooled liquid region. Our simulations show that the orientation of the shear bands with respect to the loading direction are strongly sensitive to the ambient test temperature and specimen geometry.

Finally, we show that with the aid of finite-element simulations, potential spots of damaged material can be determined from a simulated net-shape forming process of a metallic glass component.

Key words: Metallic glass, constitutive modeling, viscoplasticity, shear localization, finite-elements

1. Introduction

Recently there has been a surge in activity concerning the deformation behavior of bulk metallic glasses (BMGs). This is due to the ability in forming specimen sizes as large as a few centimeters which makes physical testing more convenient (Duine *et al.*, 1992; Peker and Johnson, 1993; Bruck *et al.*, 1994; De Hey *et al.*, 1998; Saotome *et al.*, 2001; Wang *et al.*, 2005b; Shen *et al.*, 2005) etc.

Typically forming of components e.g. micro-gear parts, biomedical devices, sporting goods, cell phone casings etc. made out of BMGs are conducted at temperatures above its *glass transition* temperature, θ_g and below its crystallization temperature, θ_x i.e. in the *supercooled liquid region*. This is because BMGs flow in a fluid-like manner within this temperature range due to having low viscosities and thus able to exhibit superplastic behavior (Saotome *et al.* (2001)). Therefore the fabrication of complicated geometries and (near) net-shape processing of BMGs can be easily performed in the supercooled liquid region. However, as shown by the experiments of Lu

*Corresponding author

Email address: mpept@nus.edu.sg (P. Thamburaja)

et al. (2003) and Wang *et al.* (2005b), shear localization and fracture of BMGs at high homologous temperatures can occur if the (absolute) applied deformation rates are large enough. Normally the applied deformation-rate to cause fracture increases with increasing ambient test temperature. Furthermore, the coupling between the deformation and temperature fields can also influence the shear localization and eventual damage process in the material. In the design of the components mentioned above, it is of paramount importance to be able to predict the location of potential damaged material points.

The characterization of shear localization and damage behavior in BMGs at high homologous temperatures have mainly been experimental work. Among recent works include the experimental efforts of Wang *et al.* (2005c) which investigate the fracture characteristics of a Zr-based BMG under tensile conditions. Wang *et al.* (2005b) have also studied the shear localization and fracture for the same Zr-based BMG under compressive loading conditions. In this work, they attribute the changing of the shear band orientation with respect to ambient test temperature is due to the variation of certain material parameters with ambient test temperatures and applied strain-rates. The influence of high temperature deformation on the fracture behavior of a Zr-based BMG was investigated by Guo *et al.* (2008). By conducting simple compression experiments under quasi-static loading rates, they attribute the suppression of plasticity (which eventually leads to fracture) at high homologous temperatures is due to aggregated nanocrystalline particles which develop during deformation. The effects of changes in ambient test temperature and loading conditions on the fracture toughness of a Zr-Based BMG has been studied by Hassan *et al.* (2008). In this work, a fracture mechanism map was developed by conducting a variety of experiments under different loading conditions ranging from room temperature to the glass transition temperature. The work of Liu *et al.* (2009) investigates the nanoscale features on fracture surfaces of a Vitreloy 1 BMG and links it to the intrinsic structure and the nature of plasticity of BMGs.

Modeling of the high homologous temperature deformation behavior of BMGs have been performed by using a fictive stress-based model (Kato *et al.*, 1998, 2001; Lu *et al.*, 2003; Kim *et al.*, 2004). The work of Huang *et al.* (2002) investigates the inhomogeneous deformation and shear localization of BMGs by developing a physically-based constitutive model. However, their constitutive model is small-strain-based in nature. Yang *et al.* (2006) have developed a finite-deformation-based constitutive model to describe the deformation behavior of BMGs under a wide rate of temperatures and deformation-rates. However, their model is not thermo-mechanically-coupled and employs the use of shear localization elements which a priori assumes the orientation of the shear bands. Recently, Thamburaja and Ekambaram (2007) have derived a thermo-mechanically-coupled, isotropic-plasticity and finite-deformation-based constitutive theory for BMGs using fundamental thermodynamic principles. They have also implemented their constitutive model into the commercially-available finite-element program ABAQUS/Explicit (2008) by writing a user-material subroutine. The modeling of the mechanical response of a Vitreloy-1 BMG at high temperatures spanning the glass transition temperature was recently conducted by Henann and Anand (2008). However, these aforementioned theories do not address the issue of damage in the material as their models do not contain a damage criterion.

Therefore, the main objectives of this work are: (1) to augment the constitutive model of Thamburaja and Ekambaram (2007); Ekambaram *et al.* (2008)) to include a damage criterion suitable for modeling the damage process in BMGs; (2) to study the shear localization and damage process for a BMG under suitable loading conditions; and (3) to simulate the net-shaping of a component made out of a BMG via finite-element simulations and to predict the locations of damaged material points.

In Section 2, we summarize the key equations in the constitutive model of Thamburaja and Ekambaram (2007) and modify it to include a damage criterion. We study the shear localization and damage process for a Vitreloy 1 BMG at temperatures within the supercooled liquid region under compressive stress states in Section 3. We use the experimental results of Lu *et al.* (2003) to calibrate the material parameters in the constitutive model. In this section, we will also attempt to simulate the net shape forming of a miniature gear part using the forming process described in Wang *et al.* (2005a). We conclude and provide directions for future works in Section 4.

2. Constitutive model

Using the methodology developed in the work of Thamburaja and Ekambaram (2007) and modifying it to include damage, we list out their key equations which describe the deformation behavior of amorphous glasses in this section. As a first-cut assumption, all the material parameters in the constitutive model are treated as constants and strictly not functions of damage (unless stated otherwise).

The governing variables¹ in the constitutive model are taken as: (i) The Helmholtz free energy per unit *reference* volume, ψ . (ii) The Cauchy stress, $\mathbf{T} = \mathbf{T}^\top$. (iii) The deformation gradient, \mathbf{F} with $\det \mathbf{F} > 0$. (iv) Absolute temperature, θ . (v) The inelastic deformation gradient, \mathbf{F}^p with $\det \mathbf{F}^p > 0$. The inelastic deformation gradient represents the cumulative deformation due to plasticity and the generation of free volume. (vi) The elastic deformation gradient, \mathbf{F}^e with $\det \mathbf{F}^e > 0$. It represents the elastic deformation that gives rise to the Cauchy stress, \mathbf{T} . Using the Kroner-Lee decomposition (Kroner (1960); Lee (1969)) the elastic deformation gradient is given by $\mathbf{F}^e = \mathbf{F}\mathbf{F}^{p-1}$. From the polar decomposition theory, we also have $\mathbf{F}^e = \mathbf{R}^e\mathbf{U}^e$ where $\mathbf{R}^e = \mathbf{R}^{e-\top}$ and $\mathbf{U}^e = \mathbf{U}^{e\top}$ represent the elastic rotation and the elastic stretch, respectively. (vii) The plastic shear strain, $\gamma \geq 0$. (viii) The free volume concentration (units of volume per unit volume), $\xi \geq 0$. (ix) The damage parameter, d with $0 \leq d \leq 1$. The value of $d = 0$ corresponds to an undamaged material point whereas a value of $d = 1$ indicates a fully-damaged material point.

2.1. Effect of damage on the elastic constants

In this work, we assume for simplicity that the damage process in metallic glasses is *isotropic* although recent work on the investigation of fracture surfaces in metallic glasses have indicated that the damage process in metallic glasses is *anisotropic* (Bouchaud *et al.*, 2008)). Further refinements of our present assumption will be made in future efforts.

Typically the elastic constants i.e. the Young's modulus and the Poisson's ratio are a function of damage. Following the work of Lemaitre (1985), we assume that the Young's modulus reduces linearly with increasing damage i.e.

$$\bar{E} = (1 - d)E \quad (1)$$

where \bar{E} and E denotes the *damaged* and *undamaged* Young's modulus, respectively. Therefore, the damaged shear modulus ($\bar{\mu}$) and bulk modulus ($\bar{\kappa}$) are respectively given by

$$\bar{\mu} = \frac{\bar{E}}{2(1 + \bar{\nu})} \quad \text{and} \quad \bar{\kappa} = \frac{\bar{E}}{3(1 - 2\bar{\nu})} \quad (2)$$

where $\bar{\nu}$ denotes the damaged Poisson's ratio.

Further assuming that the undamaged Poisson's ratio, ν is equal to the damaged Poisson's ratio i.e. $\nu = \bar{\nu}$, we substitute equation (1) into equation (2) to yield

$$\bar{\mu} = (1 - d)\mu \quad \text{and} \quad \bar{\kappa} = (1 - d)\kappa \quad \text{with} \quad \mu = \frac{E}{2(1 + \nu)} \quad \text{and} \quad \kappa = \frac{E}{3(1 - 2\nu)} \quad (3)$$

denoting the undamaged shear modulus and bulk modulus, respectively.

¹Notation : ∇ and ∇^2 denote the *referential* gradient and the *referential* Laplacian, respectively. For a second-order tensor \mathbf{B} , \mathbf{B}^\top denotes the transpose of the tensor \mathbf{B} , \mathbf{B}^{-1} denotes the inverse of the tensor \mathbf{B} , and $(\mathbf{B}^{-1})^\top = \mathbf{B}^{-\top}$. The trace of the tensor \mathbf{B} is denoted by $\text{trace}(\mathbf{B}) = \mathbf{1} \cdot \mathbf{B}$. The magnitude of tensor \mathbf{B} is denoted by $|\mathbf{B}| = \sqrt{\mathbf{B} \cdot \mathbf{B}}$. The deviatoric (traceless) portion of tensor \mathbf{B} is denoted by $\text{dev}(\mathbf{B}) = \mathbf{B} - (1/3)[\text{trace}(\mathbf{B})]\mathbf{1}$. The symmetric and skew-symmetric portion of the tensor \mathbf{B} are denoted by $\text{sym}(\mathbf{B}) = (1/2)(\mathbf{B} + \mathbf{B}^\top)$ and $\text{skew}(\mathbf{B}) = (1/2)(\mathbf{B} - \mathbf{B}^\top)$, respectively.

2.2. Free energy

With $\mathbf{E}^e = \ln \mathbf{U}^e$ and θ_o representing the elastic strain and a reference temperature, respectively, the free energy per unit *reference* volume is assumed to be in the separable form²

$$\psi = \hat{\psi}(\mathbf{E}^e, \theta, \xi, d) = \bar{\psi}^e + \psi^\theta + \psi^\xi \quad \text{where} \quad (4)$$

$$\bar{\psi}^e = \hat{\bar{\psi}}^e(\mathbf{E}^e, \theta, d) = \bar{\mu} |\text{dev}(\mathbf{E}^e)|^2 + (1/2) \bar{\kappa} [\text{trace}(\mathbf{E}^e)]^2 - 3 \bar{\kappa} \alpha_{th} (\theta - \theta_o) [\text{trace}(\mathbf{E}^e)], \quad (5)$$

$$\psi^\theta = \hat{\psi}^\theta(\theta) = c [(\theta - \theta_o) - \theta \log(\theta/\theta_o)] \quad \text{and} \quad (6)$$

$$\psi^\xi = \hat{\psi}^\xi(\theta, \xi) = (1/2) s_{\xi 1} \xi^2 - s_{\xi 1} \xi \xi_T. \quad (7)$$

The material constant α_{th} represents the coefficient of thermal expansion. The specific heat per unit *reference* volume is denoted by $c > 0$. The material parameter $s_{\xi 1} \geq 0$ (units of energy per unit volume) represents the coefficient that relate the changes in the flow-defect free energy density, ψ^ξ due to variations in ξ . Finally, ξ_T denotes the thermal equilibrium free volume concentration which can be approximated by a Vogel-Fulcher-Tammann-like linear in temperature function (Masuhr *et al.*, 1999) : $\xi_T = \xi_* + k_\theta(\theta - \theta_g)$ where k_θ is a constant of proportionality (units of temperature inverse) and ξ_* is the thermal equilibrium free volume concentration at the glass transition temperature, θ_g . Equation (5) can also be re-written as

$$\bar{\psi}^e = (1 - d) \psi^e \quad \text{with} \quad \psi^e = \mu |\text{dev}(\mathbf{E}^e)|^2 + \kappa [(1/2) \text{trace}(\mathbf{E}^e) - 3 \alpha_{th} (\theta - \theta_o)] \text{trace}(\mathbf{E}^e) \quad (8)$$

denoting the thermo-elastic free energy of an undamaged material.

2.3. Stress-strain constitutive law

The constitutive equation for the elastic stress, $\mathbf{T}^* \equiv (\det \mathbf{F}) \mathbf{R}^{e\top} \mathbf{T} \mathbf{R}^e$ is given by

$$\mathbf{T}^* = \frac{\partial \psi}{\partial \mathbf{E}^e} = 2\bar{\mu} [\text{dev}(\mathbf{E}^e)] + \bar{\kappa} [\text{trace}(\mathbf{E}^e) - 3\alpha_{th}(\theta - \theta_o)] \mathbf{1}. \quad (9)$$

2.4. Flow rule

The flow rule provides the evolution equation for the plastic deformation gradient, \mathbf{F}^p . Guided by the work of Anand and Gurtin (2003) we assume the *plastic velocity gradient*, $\mathbf{L}^p = \dot{\mathbf{F}}^p \mathbf{F}^{p-1}$ to be *irrotational* i.e. $\text{skew}(\mathbf{L}^p) = \mathbf{0}$. By decomposing the plastic velocity gradient into purely deviatoric and volumetric portions, the flow rule is then written as

$$\mathbf{L}^p = \text{sym}(\mathbf{L}^p) = \dot{\gamma} (\sqrt{1/2}) \mathbf{N} + \dot{\xi} (1/3) \mathbf{1} \quad \text{where} \quad \mathbf{N} = \frac{\text{dev}(\mathbf{T}^*)}{|\text{dev}(\mathbf{T}^*)|}. \quad (10)$$

Here $\dot{\gamma} \geq 0$ and $\dot{\xi}$ represent the plastic shear strain-rate and the free volume generation rate, respectively.

²Compared to the full expression for the free energy density in the work Thamburaja and Ekambaram (2007), we have neglected the free energy terms due to $\nabla \xi$ in this work for the sake compactness as we are assuming the size of the test specimens are several orders of magnitude larger than the length scale for free-volume diffusion.

2.5. Evolution equation for the plastic shear strain

The plastic shear strain-rate is taken as

$$\dot{\gamma} = 2\dot{\gamma}_o \sinh \left(\frac{\bar{\tau}}{s + \chi\bar{p} + \bar{\zeta}_f\bar{\tau}_v} \right). \quad (11)$$

Here $\bar{\tau} = (\sqrt{1/2}) |\text{dev}(\mathbf{T}^*)| \geq 0$ represents the *equivalent shear stress*. Guided by the work of Spaepen (1977) and modifying to include the effect of damage, the static resistance to plastic flow, $s = \hat{s}(\theta, d)$ is taken to have the following form :

$$s = (1 - d) \left[\frac{2k_b\theta}{\Omega} \right] \quad (12)$$

where k_b is the Boltzmann constant and $\Omega > 0$ the activation volume (units of volume). As shown in equation (11) the resistance to plastic flow is also affected by the *hydrostatic pressure*, $\bar{p} = -(1/3) [\text{trace}(\mathbf{T}^*)]$ and the *viscous stress*, $\bar{\tau}_v = s_{\xi 1}(\xi - \xi_T)$. The material constant χ represents the *pressure-sensitivity* parameter. We take the parameter $\bar{\zeta}_f = (1-d)\zeta_f$ where $\zeta_f > 0$ is a dimensionless fit parameter which determines the magnitude by which the plastic resistance of the undamaged material is affected by the viscous stress $\bar{\tau}_v$. Using the aforementioned expression for $\bar{\zeta}_f$ ensures that a fully-damaged material is not influenced by the effect of viscous stress.

Finally, the reference strain-rate $\dot{\gamma}_o$ is given by

$$\dot{\gamma}_o = f_o \exp \left\{ -\frac{Z}{k_b\theta} - \frac{\varphi}{\xi} \right\} \quad (13)$$

where $f_o > 0$ (units of time inverse) represents the atomic vibration frequency, $Z > 0$ the activation energy (units of energy) and $\varphi > 0$ a dimensionless geometric factor.

2.6. Kinetic equation for the free volume concentration

Neglecting free-volume diffusion, the generation of free volume occurs through free volume creation by plastic deformation, application of hydrostatic pressure, and structural relaxation. We define the material parameter $s_{\xi 2} > 0$ (units of energy per unit volume) as the *resistance* to free volume generation due to hydrostatic pressure and structural relaxation (Thamburaja and Ekambaram, 2007). Therefore, the creation-annihilation equation for the free volume concentration is given by

$$\dot{\xi} = \zeta\dot{\gamma} - \left(\frac{\dot{\gamma}_o\bar{p}}{s_{\xi 2}} \right) - \left(\frac{\dot{\gamma}_o s_{\xi 1}}{s_{\xi 2}} \right) (\xi - \xi_T). \quad (14)$$

The first term on the right-hand side of equation (14) is the creation of free volume due to plastic deformation with $\zeta = \hat{\zeta}(\mathbf{T}^*) \geq 0$ representing a dimensionless free volume creation parameter. The second term on the right-hand side of equation (14) is the generation of free volume due to hydrostatic pressure. Finally, the third term on the right-hand side of equation (14) represents the generation of free volume due to structural relaxation.

The analysis of 2004 also show the free volume creation parameter to be an increasing function of stress. Thus, for simplicity we take ζ to follow a simple piecewise functional form Thamburaja and Ekambaram (2007):

$$\zeta = \begin{cases} \zeta_c & \text{if } \bar{\tau} \leq \bar{\tau}_1 \\ \zeta_c + k_1(\bar{\tau} - \bar{\tau}_1) & \text{if } \bar{\tau} \geq \bar{\tau}_1. \end{cases}$$

Here $\zeta_c > 0$ denotes a minimum threshold value for the free volume creation coefficient, $\bar{\tau}_1 \geq 0$ a threshold equivalent shear stress and k_1 (units of stress inverse) a positive constant of proportionality.

2.7. Balance of energy and thermodynamics

From the first-law of thermodynamics, the balance equation for the temperature is

$$c\dot{\theta} = k_{th} (\nabla^2 \theta) - 3\kappa\alpha_{th} \left\{ \text{trace}(\dot{\mathbf{E}}^e) \right\} \theta - s_{\xi 1} k_{\theta} \dot{\xi} \theta + r + \dot{\omega}^p \quad (15)$$

where $k_{th} > 0$ and r represents thermal conductivity coefficient and the *referential* heat supply rate per unit volume, respectively. The rate of mechanical dissipation per unit *reference* volume, $\dot{\omega}^p$ is given by

$$\dot{\omega}^p = \bar{\tau} \dot{\gamma} - [s_{\xi 1} (\xi - \xi_T) + \bar{p}] \dot{\xi} + \psi^e \dot{d} \geq 0. \quad (16)$$

From inequality (16) we can see that the power-conjugate variable to the damage parameter is the *undamaged* thermo-elastic free energy density.

2.8. Evolution equation for the damage parameter

From phenomenological considerations, we assume that the damage and eventual fracture at a material point is possible once a critical *shear* stress for damage initiation, $\bar{\tau}_{max} = \hat{\tau}_{max}(\theta) > 0$ is reached. We let the integer i to represent a switch which indicates the possibility of damage i.e. $i = 1$ when damage is possible whereas $i = 0$ when no damage is possible. Therefore, the damage criteria can be written as :

- If $\bar{\tau} < \bar{\tau}_{max}$, then $i = 0$.
- If $\bar{\tau} \geq \bar{\tau}_{max}$, then $i = 1$.

Once the switch $i = 1$ is activated, it is maintained throughout the deformation. With the material being in the initially-undamaged state i.e. $d = 0$, we assume that damage will start to occur once the plastic shear strain, γ reaches a critical constant plastic shear strain, γ_c . The damage parameter is then taken to evolve *linearly* with the plastic shear strain, γ until a second constant critical plastic shear strain γ_f with $\gamma_f > \gamma_c$ is reached (Lemaitre, 1985)). When the plastic shear strain γ reaches γ_f the material is deemed to be fully-damaged i.e. $d = 1$. Once the material is fully-damaged, we will enforce that there can be no further increase in damage. In lieu of these conditions, we will take the damage parameter to evolve as follows :

- If $i = 1$ and $\gamma \leq \gamma_c$, then $d = 0$.
- If $i = 1$ and $\gamma_c < \gamma < \gamma_f$, then $d = \frac{\gamma - \gamma_c}{\gamma_f - \gamma_c}$.
- If $i = 1$ and $\gamma \geq \gamma_f$, then $d = 1$.

We recognize that our damage model is very simplistic. There is much work that remains in the development of more realistic fracture/damage theories to model the transition from shear localization to complete damage.

In conclusion, the list of constitutive parameters/functions needed to calibrated are

$$\{\mu, \kappa, \alpha_{th}, k_{\theta}, \xi_*, \theta_g, s_{\xi 1}, s_{\xi 2}, \chi, \zeta_c, k_1, \bar{\tau}_1, \zeta_f, f_o, \varphi, Z, \Omega, c, k_{th}, r, \bar{\tau}_{max}, \gamma_c, \gamma_f\}.$$

A time-integration procedure based on the constitutive model for metallic glasses listed above has been developed and implemented in the ABAQUS/Explicit (2008) finite-element program by writing a user-material subroutine.

3. Experiments and finite-element simulations

We study the shear localization and damage process for the compression experiments conducted by Lu *et al.* (2003) for a Vitreloy 1 metallic glass at temperatures above its glass transition temperature, $\theta_g = 623$ K. The compression test specimens have an initial cross-section area of 3.7mm by 3.7mm with its initial length being 7.4mm.

The material parameters in the constitutive model listed in Table 1 (except for $\bar{\tau}_{max}$, γ_c and γ_f) were fitted to simple compression experiments of Lu *et al.* (2003) conducted under various strain-rates at an ambient temperature of 643 K. For more details regarding the fitting procedure, please refer to Thamburaja and Ekambaram (2007).

For simplicity, we set the critical shear stress for damage initiation, $\bar{\tau}_{max}$ to be constant for temperatures above θ_g . The compression experiments of Lu *et al.* (2003) in the supercooled liquid region show an average

compressive fracture stress of approximately 1300 MPa (please see Figure 3 of Lu *et al.* (2003)). Hence, we have $\bar{\tau}_{max} = 750$ GPa. The critical plastic shear strains for fracture are set to be $\gamma_c = 0.2$ and $\gamma_f = 0.4$ for reasons we will specify later.

At an ambient temperature of 643 K, we conduct *isothermal* simple compression FEM simulations under (absolute-valued) strain-rates ranging from $2 \times 10^{-4} \text{ s}^{-1}$ to $6.5 \times 10^{-2} \text{ s}^{-1}$ using a single ABAQUS C3D8R continuum-three-dimensional brick element while assuming (1) the material is initially in the fully-annealed condition i.e. the initial free volume is at the thermal equilibrium free volume³, and (2) the deformation is *homogeneous*. These simulations and all other ensuing FEM simulations in this work were conducted using the material parameters listed in Table 1.

Table 1: List of material parameters

$\mu = 11 \text{ GPa}$	$\kappa = 35.7 \text{ GPa}$	$k_{th} = 11 \text{ W/mK}$	$c = 4.8 \text{ MJ/m}^3 \text{ K}$
$\chi = 0.15$	$\Omega = 1.49 \times 10^{-28} \text{ m}^3$	$f_o = 1.1 \times 10^{14} \text{ s}^{-1}$	$Z = 0.5 \times 10^{-19} \text{ J}$
$\theta_g = 623 \text{ K}$	$k_\theta = 13.75 \times 10^{-6} / \text{K}$	$\alpha_{th} = 10 \times 10^{-6} / \text{K}$	$\xi_* = 0.00283$
$\zeta_f = 0.045$	$\zeta_c = 9 \times 10^{-4}$	$\bar{\tau}_1 = 400 \text{ MPa}$	$k_1 = 6 \times 10^{-12} \text{ Pa}^{-1}$
$\varphi = 0.105$	$s_{\xi 1} = 10\,000 \text{ GJ/m}^3$	$s_{\xi 2} = 960 \text{ GJ/m}^3$	$\bar{\tau}_{max} = 750 \text{ GPa}$
$\gamma_c = 0.2$	$\gamma_f = 0.4$	$r = 0 \text{ J/m}^3$	

The stress-strain curves from these simulations are shown in Figure 1. With increasing strain-rate, we see increasing peak stress and steady-state stress in the stress-strain responses. The simulated results reproduces the experimental stress-strain curves to good accord⁴. Note that the initiation of damage and final fracture is only observed for the simple compression simulation conducted at an applied strain-rate of $6.5 \times 10^{-2} \text{ s}^{-1}$. This is due to the activation of the damage criteria given in Section 2.

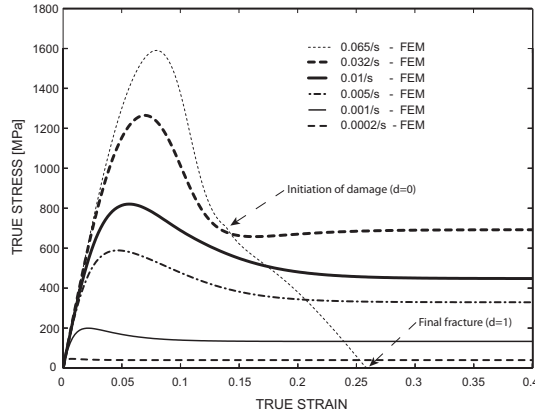


Figure 1: Simulated isothermal stress-strain response of a Vitreloy 1 BMG at an ambient temperature of 643 K in simple compression. The FEM simulation conducted at a compressive strain-rate of 0.065/s shows the initiation and progression of damage due to the activation of the damage criterion given in Section 2. Absolute values of stress and strain are plotted.

³Henceforth, all of our simulations will be conducted with the material assumed to be being initially in the fully-annealed condition i.e. the initial free volume of the material is set to be the thermal equilibrium free volume at the given ambient temperature.

⁴Please refer to the results shown in Thamburaja and Ekambaram (2007) for the comparison between the theory and experiments.

To calibrate the values for γ_c and γ_f , we perform coupled thermo-mechanical simulations on a two-dimensional cross-section of the test specimens used in the experiments of Lu *et al.* (2003). Figure 2a shows the initially-undeformed finite-element mesh of the specimen cross-section with dimensions of 3.7mm by 7.4mm measured along axis-1 and axis-2, respectively. The specimen section is meshed using 3200 ABAQUS CPE4RT continuum-two-dimensional plane-strain elements with a temperature degree of freedom. A geometrical imperfection in the specimen is introduced by providing a small taper along the length of the specimen i.e. axis-2. The temperature of the nodes on the top and bottom surfaces of the specimen is always maintained at ambient temperature throughout the duration of the simulations. Finally, a velocity profile along axis-2 (the loading axis) is imparted on the nodes on the top surface to achieve the desired test strain-rate whereas the nodes on the bottom surface are constrained from moving along axis-2.

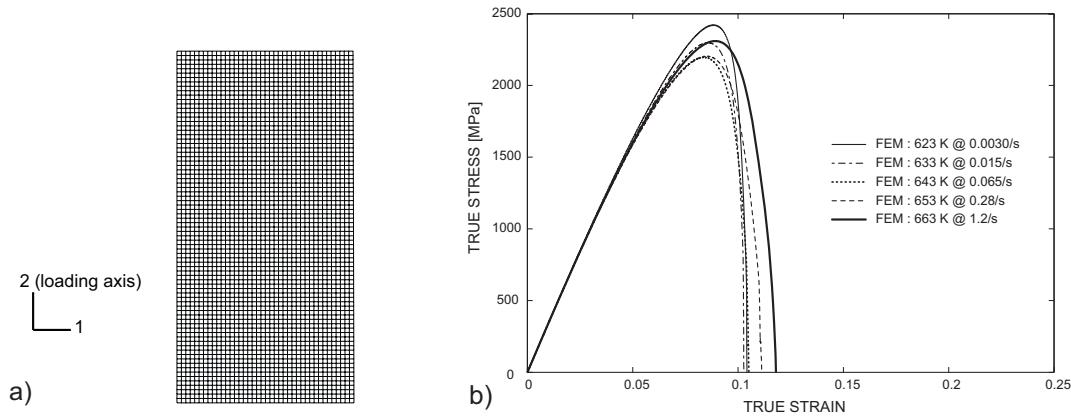


Figure 2: (a) Initially-undeformed finite-element mesh using 3200 ABAQUS CPE4RT continuum-plane-strain elements with temperature degree of freedom. A small taper along the loading axis is introduced to provide a site for geometrical imperfection. (b) Simulated stress-strain response from simulations conducted under compressive plane-strain conditions at various ambient temperatures in the supercooled liquid region. The results obtained from simulations conducted under the minimum absolute-valued applied strain-rate to cause fracture at different ambient test temperatures are shown. Absolute values of stress and strain are plotted.

The values for γ_c and γ_f are fitted to the transition locus from homogeneous to shear localization behavior as given in the experiments of Lu *et al.* (2003). In our simulations, we define the critical applied strain-rate to fracture as the absolute-valued *minimum* strain-rate which will cause a softening in the stress-strain response from a peak stress to zero stress *without* the attainment of a steady-state response⁵. Once a state of zero stress is reached in the specimen, it will no longer be able to bear any load as full damage has occurred throughout a particular cross-section of the specimen.

Using the initially-undeformed FEM mesh of the specimen section shown in Figure 2a, the stress-strain curves obtained from the coupled thermo-mechanical FEM simulations in compression conducted under different ambient temperatures are plotted in Figure 2b. From these stress-strain responses, we can see that the (absolute) critical applied strain-rate to fracture increases with increasing ambient test temperature. The variation of the critical applied strain-rate to fracture with respect to ambient test temperature is plotted in Figure 3 along with the experimental results obtained from Lu *et al.* (2003). Although the results from the constitutive model fits the overall experimentally-determined data reasonably well⁶, slight discrepancies in the fit at higher temperatures i.e. 653 K and 663 K are probably due to the over-estimation of the critical shear stress for damage initiation, $\bar{\tau}_{max}$ at these temperatures. We shall address the issue of the dependence of $\bar{\tau}_{max}$ on temperature in future works.

⁵We realize that this criterion for the selection of the minimum applied strain-rate to cause fracture is ad-hoc.

⁶Generally, γ_c and γ_f are functions of temperature. As a first-cut assumption, we will assume that γ_c and γ_f are constants. We also recognize that the values of γ_c and γ_f are not necessarily unique.

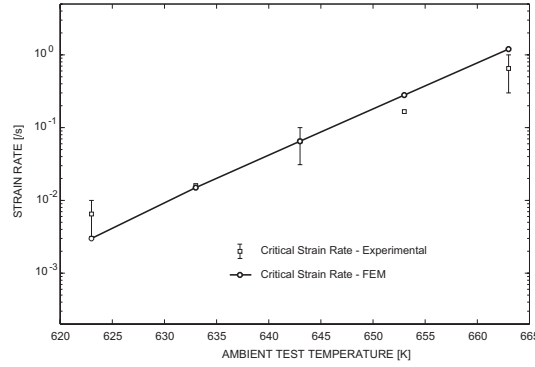


Figure 3: The simulated locus of critical (absolute) applied strain-rate to cause shear localization and fracture versus ambient test temperature. Also plotted is the experimentally-determined locus obtained from the work of Lu *et al.* (2003)).

The contours of damage at final fracture obtained from the coupled thermo-mechanical simulations performed above are plotted in Figure 4. From the contour plots shown in Figure 4, we can see that the orientation of the shear bands i.e. the fracture planes with respect to the loading axis *strongly* depends on the ambient test temperature. This finding concurs with the experimental results obtained by Wang *et al.* (2005b) for a Zr-based metallic glass at temperatures in the supercooled liquid region. The analysis of Wang *et al.* (2005b) attributes the change in the shear band orientation to the changing of the Mohr-Coulomb *friction coefficient* and the *cohesive strength* of the material with respect to the ambient temperature and testing rate. But our explanation for the changing shear band orientation with respect to the ambient test temperature is as follows: Since the applied strain-rates to cause failure at these temperatures are moderately high, the coupling between the mechanical and temperature fields become stronger (Molinari (1997)) i.e. a transient heat-transfer problem is being solved cf. equation (15). This can be verified by plotting the temperature contours in the specimen at final fracture as obtained from the coupled thermo-mechanical simulations conducted above cf. Figure 5. Comparing the results shown in Figures 4 and 5, it can be seen that the region with the largest temperature rise in the specimen coincides with the region of the shear band. From the results shown in Figure 5, we can see the utility of performing couple thermo-mechanical simulations as the magnitude of temperature rise in the shear bands are large enough such that isothermal test conditions are violated during the simulations.

However, extreme care must be taken when reporting shear band orientation for experiments conducted at temperatures within the supercooled liquid region. To illustrate this point, we repeat the coupled thermo-mechanical compression simulations performed above with the initially-undeformed finite-element mesh shown in Figure 2a having initial cross-section dimensions of 1.75mm by 3.7mm (Simulation A) and 7.4mm by 14.8 (Simulation B) instead. These two compression simulations were conducted at an ambient temperature of 623 K under an applied strain-rate of $3 \times 10^{-3} \text{ s}^{-1}$. Figures 6a and 6b respectively show the contour plots for damage and temperature obtained from Simulations A and B at the instant of final fracture in the specimen i.e. when the specimen has lost load-bearing capacity. The previously obtained result with the specimen having initial cross-section dimensions of 3.7mm by 7.4mm is also repeatedly plotted in Figure 6c for the sake of convenient comparison. From Figure 6a, we can see that the fracture plane is oriented at an angle of 43° measured with respect to the loading axis. This value for the fracture plane orientation concurs well with the experimentally-determined value from the work of Wang *et al.* (2005b) which states that fracture characteristic for experiments conducted at θ_g and temperatures well below θ_g are similar i.e. the fracture plane orientation is less than 45° when measured with respect to the loading axis. Also note that for Simulation A, the temperature rise in the shear band is about 0.3K. Therefore, the temperature conditions for specimen during the duration of the simulation are nearly *isothermal*. For Simulation B, the fracture plane is oriented at an angle of 54° measured with respect to the loading axis. Furthermore the temperature rise in the shear band from Simulation B is approximately 58K i.e. isothermal test conditions in the specimen are not achieved during the duration of the simulation. The simulation results shown in Figure 6c also show different orientation of the fracture plane and

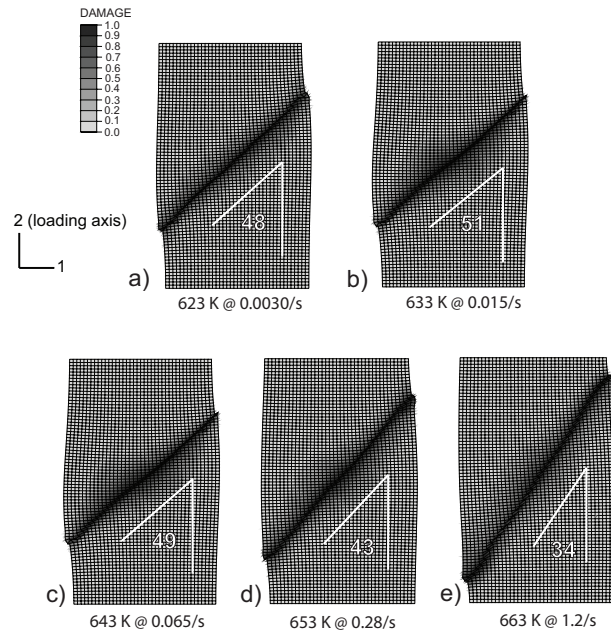


Figure 4: Simulated contours of damage plotted for the specimen at the first instance when damage has spread throughout the cross-section of the specimen i.e. when the specimen has lost the ability to bear load. These contours were determined from the FEM simulations which provided the stress-strain curves as plotted in Figure 3b. Also shown is the applied strain-rate imposed on the specimen along with the ambient test temperature. The orientations of the shear bands with respect to the loading direction are also shown.

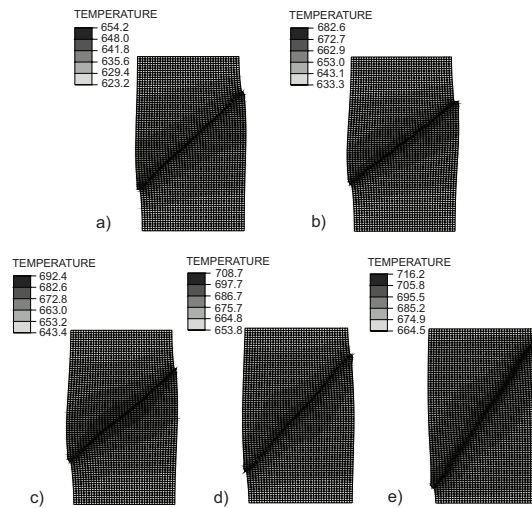


Figure 5: Simulated contours of temperature in the specimen obtained from the plane-compression compression simulation conducted at an (absolute) applied strain-rate and ambient test temperature of (a) 0.003/s at 623K, (b) 0.015/s at 633K, (c) 0.065/s at 643K, (d) 0.28/s at 653K, and (e) 1.2/s at 663K. Figures 5a to 5e are plotted at the same instance when Figures 4a to 4e are plotted, respectively.

temperature rise in the shear band as compared to the results obtained from Simulations A and B.

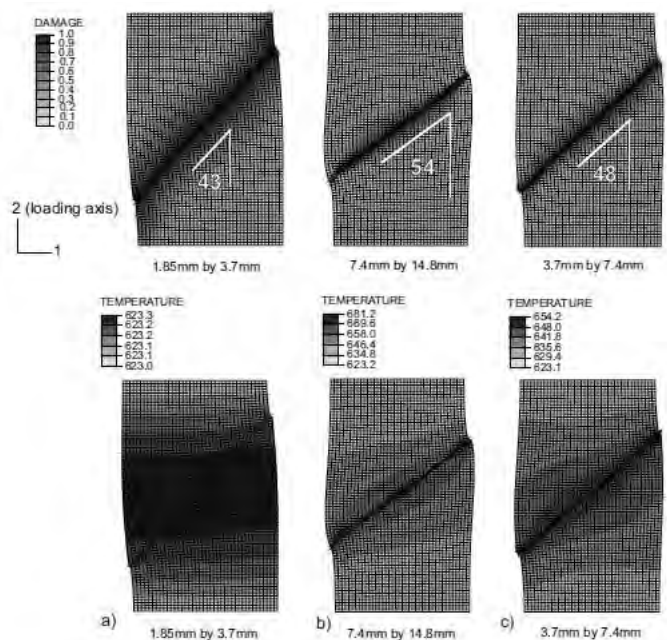


Figure 6: Simulated contours of damage and temperature for a specimen with initial cross-section dimensions of (a) 1.85mm by 3.7mm, (b) 7.4mm by 14.8mm, and (c) 3.7mm by 7.4mm. These contours were plotted at the first instance when the specimens have lost its ability to bear load. All these simulations were conducted at an ambient temperature of 623K under an applied compressive strain-rate of 0.003/s. The orientations of the shear bands with respect to the loading direction are also shown.

Therefore, we can conclude from the results plotted in Figure 6 that the orientation of the fracture plane measured with respect to the loading axis is also *strongly* dependent on the specimen dimensions. This is to be expected since, as mentioned previously, a transient heat transfer problem is being solved during the coupled thermo-mechanical simulations i.e. the heat conduction term in equation (15) introduces a *length-scale* into the energy balance equation. This inherent length scale is responsible for the observed sensitivity of the fracture plane orientations to the specimen dimensions⁷. To the best of our knowledge, the present work is the first of its kind in characterizing the *shear localization* and *fracture* behavior in metallic glasses at temperatures in the *supercooled liquid region*.

3.1. (Near)net-shape forming of a bulk-metallic glass component

The superplastic forming of components made out of bulk-metallic glasses are typically conducted at temperatures in the supercooled liquid region Saotome *et al.* (2001) and Wang *et al.* (2005a). This is done because metallic glasses exhibit fluid-like properties and flows very easily when deformed in this temperature regime. Hence net-shape forming can be easily achieved when metallic glasses are deformed at temperatures above θ_g .

In this work, we will simulate the net-shape forming of a metallic glass sample into a micro-gear component. As an example, we will assume that this metallic glass sample has the same material properties as listed in Table 1. The geometry for the micro-gear forging mould is taken from the work of Wang *et al.* (2005a) and is shown in Figure 7a. Also shown in Figure 7a is the initial geometry for the cylindrically-shaped metallic glass workpiece. Due to the symmetry of the forming process, we will only model 1/12-th of an initially-cylindrical metallic glass workpiece and the forging mould. Figure 7b shows the initially-undeformed mesh of the metallic glass workpiece

⁷In fact, the orientation of the shear bands are also very sensitive to the thermal conductivity coefficient, k_{th} .

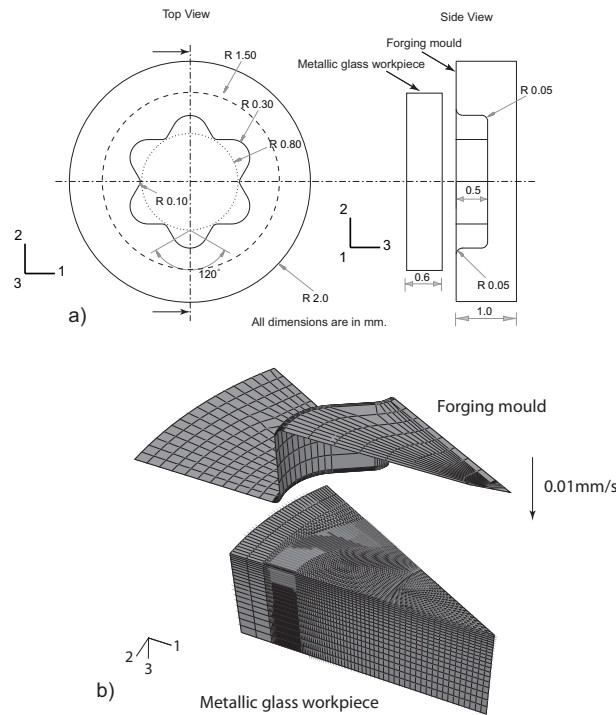


Figure 7: (a) Initial geometry of the micro-forging mould and the metallic glass workpiece obtained from the work of Wang *et al.* (2005c). (b) Initially-undeformed finite-element mesh of the forging mould (meshed using 1002 ABAQUS R3D4 rigid elements) and the metallic glass workpiece (meshed using 64560 ABAQUS C3D8R elements). Due to symmetry, we only mesh and simulate 1/12-th of the whole ensemble as shown in Figure 7a.

and the forging mould. The metallic glass workpiece is meshed using 64560 ABAQUS C3D8R elements. The forging mould is idealized as being a rigid body and it is meshed using 1002 ABAQUS R3D4 rigid elements. The whole ensemble is kept at a constant temperature of 663K and we assume that isothermal conditions prevail throughout the duration of the simulation. The nodes on the bottom of the metallic glass workpiece is prevented from having motion along axis-3. The rigid forging mould is then pressed into the metallic glass workpiece at a speed of 0.01mm/s along axis-3 with its other degrees of freedom being suppressed.

Figure 8 shows the simulated forging load versus the displacement of the forging mould once the forging mould comes into contact with the metallic glass specimen. Figures 8a to 8f show the geometry of the micro-gear respectively keyed to points a to f on the force-displacement curve shown in the same figure. Also plotted on the geometry of the micro-gear are the contours of damage in the metallic glass specimen. As shown in Figure 8f, the forging mould is fully-filled once point f is reached on the force-displacement response. Hence net-shape forming of the micro-gear component has been achieved at this point. The simulations are also able to predict the areas in the micro-gear which are damaged once the forming process is completed cf. Figure 8f. Thus our simulations can be used as a tool to aid in the design process of metallic glass specimens undergoing superplastic forming by identifying potential failure spots.

4. Conclusion and future work

The coupled thermo-mechanical, three-dimensional and finite-deformation-based constitutive equations for metallic glasses developed by Thamburaja and Ekambaram (2007) which have been modified to include a damage criterion has been shown to be capable of modeling the shear localization and eventual fracture process in metallic glass specimens tested at temperatures within the supercooled liquid region.

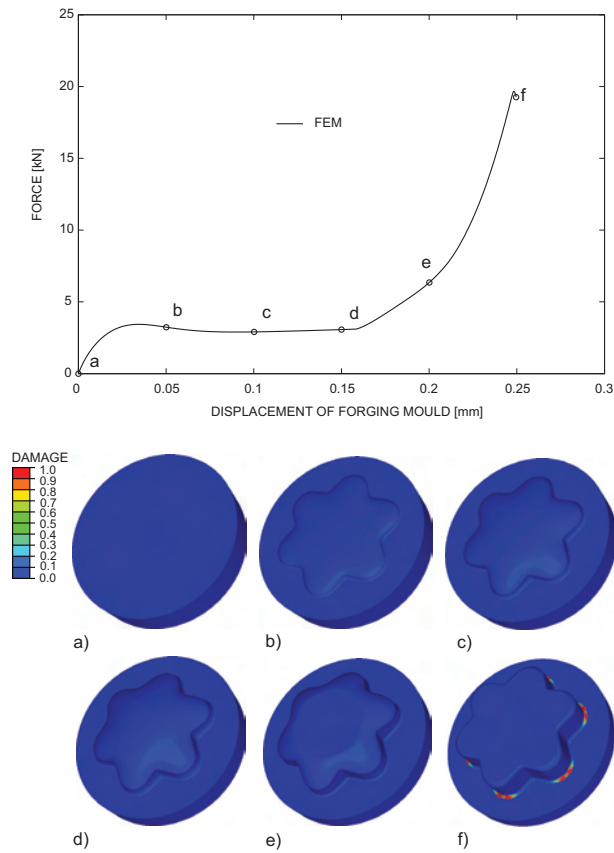


Figure 8: Simulated forging force versus mould displacement for the forging simulation described in Section 3.1. The simulated contours of damage plotted on the metallic glass workpiece keyed to points *a* to *f* on the force-displacement curve are also shown.

Furthermore, the present work also shows that the orientation of shear bands (fracture planes) with respect to the loading direction under compressive stress-states is strongly dependent on the ambient test temperature and specimen geometry. This is to be expected since a transient heat transfer problem is solved during the deformation of the metallic glass i.e. the heat conduction term in the energy balance equation introduces a length-scale into the theory.

Some future works include the modeling of physical experiments conducted under multi-axial loading conditions e.g. forming, three-point bending etc. These experiments are to be conducted under a variety of temperatures and deformation rates.

Acknowledgements

The financial support for this work was provided by the Ministry of Science, Technology and Innovation, Malaysia under Grant 03-01-02-SF0257. The ABAQUS finite-element software was made available under an academic license from SIMULIA.

References

Anand, L. and Gurtin, M. (2003). A theory of amorphous solids undergoing large deformations, with application to polymeric glasses, *International Journal of Solids and Structures* **40**, pp. 1465–1487.

- Bouchaud, E., Boivin, D., Pouchou, J., Bonamy, D., Poon, B. and Ravichandran, G. (2008). Fracture through cavitation in a metallic glass, *Europhysics Letters* **83**, p. 66006.
- Bruck, H., Christman, T., Rosakis, A. and Johnson, W. (1994). Quasi-static constitutive behavior of zr-ti-cu-ni-be bulk amorphous alloy, *Scripta Metallurgica et Materiala* **30**, pp. 429–434.
- De Hey, P., Sietsma, J. and Van Den Beukel, A. (1998). Structural disordering in a amorphous pd-ni-p induced by high temperature deformations, *Acta Materialia* **46**, pp. 5873–5882.
- Duine, P., Sietsma, J. and van den Beukel, A. (1992). Defect production and annihilation near equilibrium in amorphous pd-ni-p investigated from viscosity data, *Acta Metallurgica Materialia* **40**, pp. 743–751.
- Ekambaram, R., Thamburaja, P. and Nikabdullah, N. (2008). On the evolution of free volume during the deformation of metallic glasses at high homologous temperatures, *Mechanics of Materials* **40**, pp. 487–506.
- Guo, B., Guo, X., Ma, M., Shan, D. and Zhang, W. (2008). Influence of high temperature deformation on the fracture behavior of a bulk zr-based metallic glass, *Journal of Non-Crystalline Solids* **354**, pp. 3348–3353.
- Hassan, H., Kecskes, L. and Lewandowski, J. (2008). Effects of changes in test temperature and loading conditions on fracture toughness of a zr-based bulk metallic glass, *Metallurgical and Materials Transactions A* **39**, pp. 2077–2085.
- Heggen, M., Spaepen, F. and Feuerbacher, M. (2004). Plastic deformation of pd-ni-cu bulk metallic glass, *Materials Science and Engineering A* **375-377**, pp. 1186–1190.
- Henann, D. and Anand, L. (2008). A constitutive theory for the mechanical response of amorphous metals at high temperatures spanning the glass transition temperature: Application to microscale thermoplastic forming, *Acta Materialia* **56**, pp. 3290–3305.
- Huang, R., Suo, Z., Prevost, J. and Nix, W. (2002). Inhomogeneous deformation in metallic glasses, *Journal of the Mechanics and Physics of Solids* **50**, pp. 1011–1027.
- Kato, H., Kawamura, Y., Inoue, A. and Chen, H. (1998). Newtonian to non-newtonian master flow curves of a bulk glass alloy pd-ni-cu-p, *Applied Physics Letters* **73**, pp. 3665–3667.
- Kato, H., Kawamura, Y., Inoue, A. and Chen, H. (2001). Modeling of stress-strain curves for pd-ni-cu-p glass alloy under constant strain-rate deformation, *Materials Science and Engineering A* **304**, pp. 758–762.
- Kim, H., Kato, H., Inoue, A., Chen, H. and Hong, S. (2004). Microforming of bulk metallic glasses : Constitutive modelling and applications, *Materials Transactions - JIM* **45**, pp. 1228–1232.
- Kroner, E. (1960). Allgemeine kontinuumstheorie der versetzungen und eigenspannungen, *Archive for Rational Mechanics and Analysis* **4**, pp. 273–334.
- Lee, E. (1969). Elastic plastic deformation at finite strain, *Journal of Applied Mechanics* **36**, pp. 1–6.
- Lemaitre, J. (1985). Coupled elasto-plasticity and damage constitutive equations, *Computer Methods in Applied Mechanics and Engineering* **51**, pp. 31–49.
- Liu, L., Zhang, H., Li, H. and Zhang, G. (2009). Nanoscale morphologies on the fracture surface of bulk metallic glasses in the supercooled liquid region, *scripta materialia* **60**, pp. 795–798.
- Lu, J., Ravichandran, G. and Johnson, W. (2003). Deformation behavior of the zr-ti-cu-ni-be bulk metallic glass over a wide range of strain-rates and temperatures, *Acta Materialia* **51**, pp. 3429–3443.
- Masuhr, A., Busch, R. and Johnson, W. (1999). Thermodynamics and kinetics of the zr-ti-cu-ni-be bulk metallic glass forming liquid: glass formation from a strong liquid, *Journal of Non-Crystalline Solids* **252**, pp. 566–571.
- Molinari, A. (1997). Collective behavior and spacing of adiabatic shear bands, *Journal of the Mechanics and Physics of Solids* **45**, pp. 1551–1575.
- Peker, A. and Johnson, W. (1993). A highly processable metallic glass : Zr-ti-cu-ni-be, *Applied Physics Letters* **63**, pp. 2342–2344.
- Saotome, Y., Hatori, T., Zhang, T. and Inoue, A. (2001). Superplastic micro/nano-formability of $\text{la}_{60}\text{al}_{20}\text{ni}_{10}\text{co}_5\text{cu}_5$ amorphous alloy in supercooled liquid state, *Materials Science and Engineering A* **304-306**, pp. 716–720.
- Shen, J., Wang, G., Sun, J., Stachurski, Z., Yan, C., Ye, L. and Zhou, B. (2005). Superplastic deformation behavior of zr-ti-ni-cu-be bulk metallic glass in the supercooled liquid region, *Intermetallics* **13**, pp. 79–85.
- Thamburaja, P. and Ekambaram, R. (2007). Coupled thermo-mechanical modelling of bulk-metallic glasses : Theory, finite-element simulations and experimental verification, *Journal of the Mechanics and Physics of Solids* **55**, pp. 1236–1273.

- Wang, G., Shen, J., Sun, J., Huang, Y., Zou, J., Lu, Z., Stachurski, Z. and Zhou, B. (2005a). Superplasticity and superplastic forming ability of a zr-tin cube bulk metallic glass in the supercooled liquid region, *Journal of Non-Crystalline Solids* **351**, pp. 209–217.
- Wang, G., Shen, J., Sun, J., Lu, Z., Stachurski, Z. and Zhou, B. (2005b). Compressive fracture characteristics of a zr-based bulk metallic glass at high test temperatures, *Materials Science and Engineering A* **398**, pp. 82–87.
- Wang, G., Shen, J., Sun, J., Lu, Z., Stachurski, Z. and Zhou, B. (2005c). Tensile fracture characteristics and deformation behavior of a zr-based bulk metallic glass at high temperatures, *Intermetallics* **13**, pp. 642–648.
- Yang, Q., Mota, A. and Ortiz, M. (2006). A finite-deformation constitutive model of bulk metallic glass plasticity, *Computational Mechanics* **37**, pp. 194–204.